Article

Optical Imaging and Analytical Design of Localized Topological Structures in Chiral Liquid Crystals

Igor Lobanov [1,*] , **Elena Aksenova** [2] , **Tetiana Orlova** [3] , **Darina Darmoroz** [3] , **Valery Uzdin** [1,2]
and Alexei D. Kiselev [4,*]

1 School of Physics and Engineering, ITMO University, Kronverksky Pr. 49, Saint Petersburg 197101, Russia
2 Faculty of Physics, Saint Petersburg State University, 7-9 Universitetskaya Emb.,
   Saint Petersburg 199034, Russia
3 Infochemistry Scientific Center, ITMO University, Lomonosova Str. 9, Saint Petersburg 191002, Russia
4 Laboratory of Quantum Processes and Measurements, ITMO University, Kadetskaya Line 3b,
   Saint Petersburg 199034, Russia
* Correspondence: igor.lobanov@metalab.ifmo.ru (I.L.); adkiselev@itmo.ru (A.D.K.)

Abstract: We combine numerical modeling and analytical design techniques to study several of the most common localized topological structures in frustrated chiral nematic liquid crystal cells. An energy minimization procedure is applied to the lattice model to simulate the director field distributions. These distributions are also approximated using the suitably designed analytical ansatz. We present both simulated and approximated results for optical polarizing microscopy textures and different visualizations of director field structure such as distributions of the azimuthal director angle and isolines for the normal component of the director in coordinate planes. The ansatz correctly mimicked the geometry and optical properties of the solitonic structures under consideration.

Keywords: localized topological structures; chiral liquid crystals; 3D soliton; skyrmion; optical imaging

1. Introduction

Chiral nematic (cholesteric) liquid crystals (CLCs) host numerous topological solitons represented by localized chiral liquid crystal structures. In experiments, the localized chiral structures manifest themselves as optically inhomogeneous patterns. For the structures known as cholesteric spherulites or cholesteric bubbles, such patterns have long been observed in CLCs [1,2].

In cholesteric liquid crystal cells, solitonic structures may appear as a result of frustration. The latter comes into play when chirality favoured effects leading to a macroscopic twist in the orientation of the liquid crystal (LC) molecules compete with other influences on the CLC system, such as external fields and constraints imposed by either geometry or boundary conditions. These localized structures have already been exploited as individual micron-sized elements for refractive and singular optics [3–5], components of diffraction gratings [6], and transport micromachines [7–9].

The formation of localized structures is ensured by the metastability of orientational structures in CLCs confined in the slab geometry with homeotropic anchoring condi-tions (preferred orientation of the LC molecules at the boundary is normal to the sub-strates) [10–13]. When the ratio of the cell thickness and the equilibrium CLC pitch (this is the helix pitch describing twisted equilibrium structures in an unbounded LC sample) is be-low its threshold value, the cholesteric helix is completely unwound, and the ground-state structure is uniform. However, when an external stimulus is applied, producing sufficiently large perturbations of the uniform frustrated state and leading to the formation of solitons, the localized chiral structures may persist even after switching off the stimulus.

One of the standard methods is to use short pulses of an electric/optical field as external stimuli inducing the local reorientation of a cluster of molecules [1,2,6,14–16].

Another approach, employed in [17] to generate cholesteric bubbles, is to combine heating the CLC sample up to the transition to an isotropic phase with subsequent rapid cooling down. The third method, demonstrated in [18,19], involves the control of the helicoidal periodicity at the molecular scale by light [20], and allows for the generation of dynamic localized chiral structures in addition to the well-studied static ones.

The main feature of the localized chiral structures is their nontrivial topology or the three dimensional (3D) spatial organization of the LC director field [14,21]. The so-called toron is probably the smallest chiral topological structure with a diameter close the thickness of the LC cell. The topology of the toron can be described as a double-twisted supramolecular cylinder lying in the plane of the sample, surrounded from above and below by a pair of hyperbolic point defects [15]. By contrast, a loop of the first-kind cholesteric finger (CF1) with two pairs of nonsingular disclinations can be regarded as the topologically simplest 3D solitonic structure [22–24]. Its decrease in size leads to the formation of a localized structure without a uniform central part. A two-dimensional (2D) optical microscopic image of this structure appears to be chiral [16,18,23,24], and the director field distribution behind such optical view can be obtained by shrinking one of the disclination lines into a point defect [25].

The 3D molecular architecture underlying the complex topology of localized chiral structures cannot be reconstructed solely from two dimensional optical microscopy images. Usually, a powerful fluorescence confocal polarizing microscopy (FCPM) technique is applied to visualize the LC director field in three dimensions [26,27]. Other methods, such as multiharmonic generation microscopy or stimulated Raman scattering microscopy, are also employed to reconstruct 3D molecular organization.

Each of the above methods has its own disadvantages [28]. FCPM implies the doping of a LC with fluorescent molecules whose orientation with respect to the LC director must be unambiguous. Chemically selective Raman microscopy requires a fixed bond orientation of a certain chemical group within molecules. Thus, 2D optical microscopy imaging may still be useful for the initial inspection of CLC structures in order to identify unusual director field patterns for the further analysis of 3D molecular ordering.

In this paper, our approach is based on the method where analytically approximated orientational configurations are used for solitonic structure engineering in combination with simulated polarized optical microscopy (POM) textures. By using the free energy minimization procedure applied to the lattice model derived as a discretization of the LC free energy functional, we obtain three localized chiral structures of different topologies resembling chiral 3D patterns often observed in experiments [14,16,18,19,24,25,29–31] and demonstrate how this method can be used to clarify primitive building blocks underlying the architecture of director fields. We show that the ansatz formulated in terms of looped CF1 cholesteric fingers of different diameters suffices to reconstruct both the 3D orientational configurations and 2D optical images. The paper is organized as follows.

In Section 2, we briefly comment on numerical modeling techniques employed to simulate the director field distributions and POM textures. The simulation results representing target structures are detailed in Section 3.1. The analytical modeling procedure that uses the director field ansatz to approximate the structures is described in Section 3.2. Our results for simulated and approximated structures are presented in Section 3.3, and we present some concluding remarks in Section 4.

2. Materials and Methods

2.1. Frank Free Energy

The topological solitons in CLCs are 3D orientational structures determined by the CLC director field **n** (a unit vector specifying local preferred orientation of LC molecules) within the CLC sample of the volume V. An important point is that CLCs are optically anisotropic liquids with locally uniaxial optical anisotropy defined by the optical axis orientated along the director field.

The continuum theory of CLCs is formulated in terms of the Frank–Oseen free energy functional that, in the absence of external fields, takes the following form (see, e.g., the book [32]):

$$F[\mathbf{n}] = \int_V d\mathbf{r}\,\omega(\mathbf{r}),$$

$$\omega(\mathbf{r}) = \frac{K_1}{2}(\nabla \cdot \mathbf{n})^2 + \frac{K_2}{2}(\mathbf{n} \cdot \nabla \times \mathbf{n} + q)^2 + \frac{K_3}{2}(\mathbf{n} \times \nabla \times \mathbf{n})^2, \tag{1}$$

where $\omega(\mathbf{r})$ is the elastic free energy density; K_1, K_2, K_3 are the splay, twist, and bend Frank elastic constants, respectively; q is the free twisting number inversely proportional to the equilibrium CLC pitch, P: $q = 2\pi/P$. In addition to the bulk part of the CLC energy, there is the surface contribution to the energy. It is expressed in terms of the surface energy density known as the anchoring energy that dictate the anchoring conditions at bounding surfaces.

We consider the case of the slab geometry where CLC is placed between two parallel bounding plates (substrates), $z = -L/2$ and $z = L/2$, where L is the cell thickness, and assume that the anchoring conditions are homeotropic and strong. In other words, our boundary conditions require the director orientation at the substrates to be fixed along the normal to the cell (the z axis). This is the limiting case of strong anchoring where the surface elasticity contributions such as the K_{24} term can be neglected.

Director distributions representing metastable CLC structures can be found by minimizing the elastic free energy F (1). Dynamics of director reorientation is governed by the dynamic equation of the following form:

$$\frac{d\mathbf{n}}{dt} = -\eta\,\frac{\delta F[\mathbf{n},q]}{\delta \mathbf{n}}, \tag{2}$$

where η is the rotational viscosity that plays the role of the relaxation rate constant and $\dfrac{\delta F}{\delta \mathbf{n}}$ is the functional derivative of the free energy functional with respect to the director that can be written in the explicit form as follows:

$$\frac{\delta F[\mathbf{n},q]}{\delta \mathbf{n}} = -K_1\nabla(\nabla \cdot \mathbf{n}) - K_3[\Delta\mathbf{n} - \nabla(\nabla \cdot \mathbf{n})]$$
$$+ (K_2 - K_3)[2(\mathbf{n} \cdot \nabla \times \mathbf{n})(\nabla \times \mathbf{n}) - \mathbf{n} \times \nabla(\mathbf{n} \cdot \nabla \times \mathbf{n})] + K_2(2q\nabla \times \mathbf{n} - \mathbf{n} \times \nabla q). \tag{3}$$

Equation (2) gives the simplified model of CLC director dynamics where the coupling between the director and the fluid flow is assumed to be negligible. However, in our case, this model is used within the context of relaxation methods, so that the steady-state solution to Relaxation Problem (2) gives the metastable state of the system corresponding to the local minimum of the free energy.

As in [33], our overall computational strategy involves two basic steps: (a) we introduce a properly discretized version of the free energy (1), and (b) we employ the direct energy minimization by the nonlinear conjugate gradient method [34,35] in Cartesian coordinates with constraints that fix the unit length of the director at the sites of the lattice. Geometry of our lattice model is similar to that presented in [33]: directors are localized at the points of a simple cubic lattice inside the rectangular cell where both lateral sizes (the lengths along the x and y axes) are equal to L_W. In contrast to [33], in this paper, we go beyond the scope of the one-constant approximation.

In our calculations, the liquid crystal mixture E7 LC with the Frank constants $K_1 = 10.5$ pN [36], $K_2 = 6.2$ pN, $K_3 = 18.7$ pN [36–39] was used as a model LC material. In the lattice model, the number of points along the normal and along each lateral direction are 40 and 240, respectively (the total number of points is 2,304,000). The cell thickness was $L = 10$ μm, whereas both the lateral sizes of the CLC cell are equal to $L_W = 60$ μm.

2.2. Optical Imaging of Localized Topological Structures

As mentioned above, the optical anisotropy of CLC is locally uniaxial with the optical axis directed along the director field, $\mathbf{n}(\mathbf{r}) \equiv \mathbf{n}(x, y, z)$. The optical properties of such media are governed by the optical dielectric tensor of the following form:

$$\epsilon_{ij} = \epsilon_{\perp} \delta_{ij} + (\epsilon_{\parallel} - \epsilon_{\perp}) n_i n_j, \tag{4}$$

where $i, j \in \{x, y, z\}$, δ_{ij} is the Kronecker symbol, and n_i is the ith component of the CLC director, $\epsilon_{\perp}$ and $\epsilon_{\parallel}$ are the principal values of the tensor that define the ordinary and extraordinary refractive indices: $n_o = \sqrt{\mu \epsilon_{\perp}}$ and $n_e = \sqrt{\mu \epsilon_{\parallel}}$ (in what follows, the magnetic tensor of the CLC is assumed to be isotropic with the magnetic permittivity $\mu \approx 1$).

Thus, in order to compute 2D distributions of light intensities representing the polarized optical microscopy textures (images), we utilize both the director field evaluated at the points of our lattice model and the optical tensor (4) with refractive indices n_o and n_e. In our calculations we consider the case of normally incident light and employ the well-known Jones matrix method [40,41]. According to this method, an LC sample with a localized topological structure is split into a set of thin slabs with the director orientation patterns obtained by either numerical or analytical modeling. The effect of the jth thin slab is represented by a phase retardation plate with the optical axis that varies in the lateral plane: $\mathbf{n}(x, y, j\Delta z) = (\sin\theta_j(x,y)\cos\phi_j(x,y), \sin\theta_j(x,y)\sin\phi_j(x,y), \cos\theta_j(x,y))$. This can be described by a coordinate-dependent Jones matrix [40,41] of the following form:

$$\mathbf{J}_i = \mathbf{R}^{-1}(\phi_j(x,y)) \begin{pmatrix} e^{i\Gamma_j(x,y)}, 0 \\ 0, e^{-i\Gamma_j(x,y)} \end{pmatrix} \mathbf{R}(\phi_j(x,y)), \quad \mathbf{R}(\phi_j) = \begin{pmatrix} \cos\phi_j & -\sin\phi_j \\ \sin\phi_j & \cos\phi_j \end{pmatrix},$$

$$\Gamma_j(x,y) = \frac{\pi(n_{\text{eff}}(\theta_j(x,y)) - n_o)\Delta z}{\lambda}, \quad n_{\text{eff}}(\theta_j) = \frac{n_o n_e}{\sqrt{n_o^2 \cos^2\theta_j + n_e^2 \sin^2\theta_j}}. \tag{5}$$

Formula (5) implies that, while propagating through the CLC cell, light splits into ordinary and extraordinary waves. These waves "feel" the ordinary refractive index n_o and the effective extraordinary refractive index $n_{\text{eff}}(\theta)$ dependent on the angle θ between $\mathbf{n}$ and the normal to the substrates giving the light's propagation direction, respectively [40,41]. Given the linearly polarized incident wave, the intensity of the transmitted light at each pixel of a computed POM texture (image) is evaluated by successive multiplication of the Jones matrices corresponding a series of thin CLC slabs with the coordinate-dependent phase retardation and an analyzer.

To mimic achromatic-light observations, we performed these calculations for wavelengths 450, 530, and 650 nm, and then superimposed the resulting textures to obtain a POM image between crossed linear polarizers for white imaging light.

3. Results

3.1. Simulated Structures

Our simulation procedure employed to generate localized topological structures begins with constructing state S3 as a closed loop of the CF1 cholesteric finger whose orientational structure is well-known [42,43]. To this end, we used an analytically approximated orientational structure as the initial state and performed the relaxation procedure described in Section 2.1 that ensured the formation of metastable structure S3. Details on analytical approximations are given in the subsequent Section 3.2 (see Equation (16)). With the model parameters described at the end of Section 2.1, we obtained the metastable S3 structure at the CLC helix pitch $P = 9.0$ μm.

At the next step, we changed the helix pitch to $P = 10.0$ μm and restarted the relaxation procedure. In the process of relaxation, we observed the formation of transient structure TS2, and structure S1 became the final stage of relaxation. Figure 1 shows localized structures

S3, TS2, and S1 resulting from the described procedure. They bear close resemblance to localized chiral structures reported in a number of experiments [14–16,18,23–25,31,42].

White-light POM textures (a) and (b) are computed using the Jones matrix method briefly described in Section 2.2 for the cases of high (Figure 1a) and low (Figure 1b) bire-fringence, $\Delta n = n_e - n_o$. The director distributions in the xy and xz planes are illustrated in Figure 1c,d, respectively. In all such distributions, we assumed that the cross-sections passed through the center of the cell, and the color encoded the azimuthal director orientation (orientation of the director projection onto the xy plane). In all figures, the colors are defined over the whole sphere of director orientations. The color wheels show that, in the northern hemisphere where the z projection of the director is located, n_z, is non-negative, the colors become lighter as n_z approaches unity (the northern pole is white). By contrast, in the southern hemisphere, the colors darken as n_z decreases approaching the southern pole with $n_z = -1$. The obtained director fields for TS2 and S1 are later used as target orientational structures to be approximated using the ansatz.

The relaxation of state S3 involves continuous transformations most vividly manifested by shrinking of the structure. There are three qualitatively different types of states that can be distinguished in the course of relaxation. At the initial stage, similar to the CF1 loop patterns reported in [16,23,24,42], the POM image of the structure S3 contains a black region in the center corresponding to the uniform director orientation. As is shown in Figure 2, the topological structure of the director field is represented by four closed disclination lines: two pairs of $\lambda^{+1/2}$ and $\lambda^{-1/2}$ disclinations [42,43].
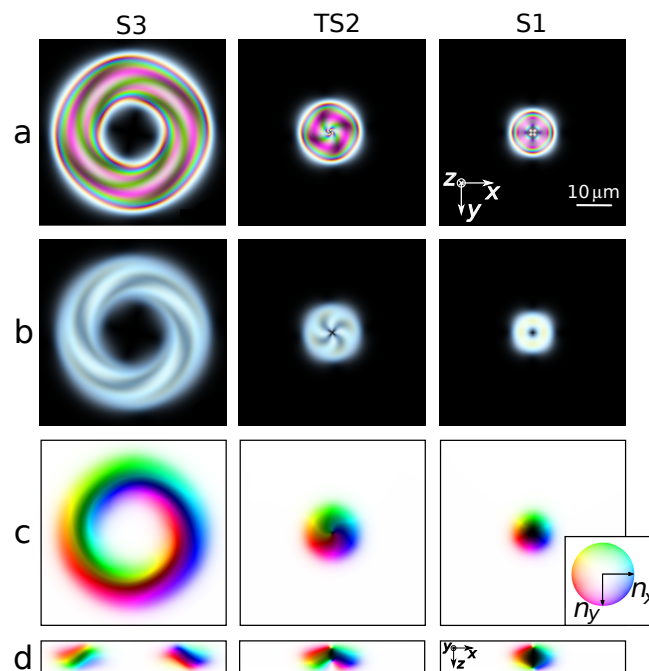

Figure 1. POM textures and director distributions for solitonic CLC structures S1, TS2, and S3. (**a**) White light POM textures in crossed polarizers computed at $n_e = 1.76$ and $n_o = 1.53$ [44]. Orientation of the axes for (**a**–**c**) and the white scale bar for all figures are shown in the inset at the left and the right of the texture for S1, respectively. (**b**) White light POM textures in crossed polarizers computed for the case of low birefringence with $n_e = 1.55$ and $n_o = 1.47$ [44]. (**c**) Director field distributions in the xy plane (the middle cross-section of the cell at $z = 0$). The color palette in the inset at the right of the director distribution for S1 describes x and y projections of the director used in (**c**,**d**). This color wheel represents the northern hemisphere of director orientations where n_z is non-negative. In the southern hemisphere, the colors become darker as n_z decreases approaching the southern pole with $n_z = -1$. (**d**) Director field distributions in the xz plane with the origin placed at the center of the sample. Orientation of the axes is shown in the inset at the left of the distribution for S1.

At the next stage, when the central black region disappears keeping the spiral arms intact, the structure called TS2 is formed. Though POM textures for the TS2 pattern resembles those observed in [16,19,25], in our case, this structure is transient. Referring to Figure 2, topology of the TS2 structure is described by the only disclination line and a pair of hyperbolic point defects (hyperbolic hedgehogs). Clearly, the disclination charge is twice as large as that for the disclinations characterizing the S3 structure. In general, TS2 might be described as an extrachiral toron structure [14,15] that is chiral not only in terms of an orientational structure, but also in terms of a 2D optical view.

Even though we did not observe qualitative changes in the POM images at this stage, transient structures may somehow differ in topology owing to transitions between disclinations and point defects. In our subsequent theoretical considerations, we consider the TS2 structure as a target state representing transient structures whose POM images are qualitatively similar.

At the final stage, the spiral arms in the POM texture disappeared, and metastable state S1 was formed. The topology of the director field of this state is illustrated in Figure 2. It represents the well-known toron structure [1,15].
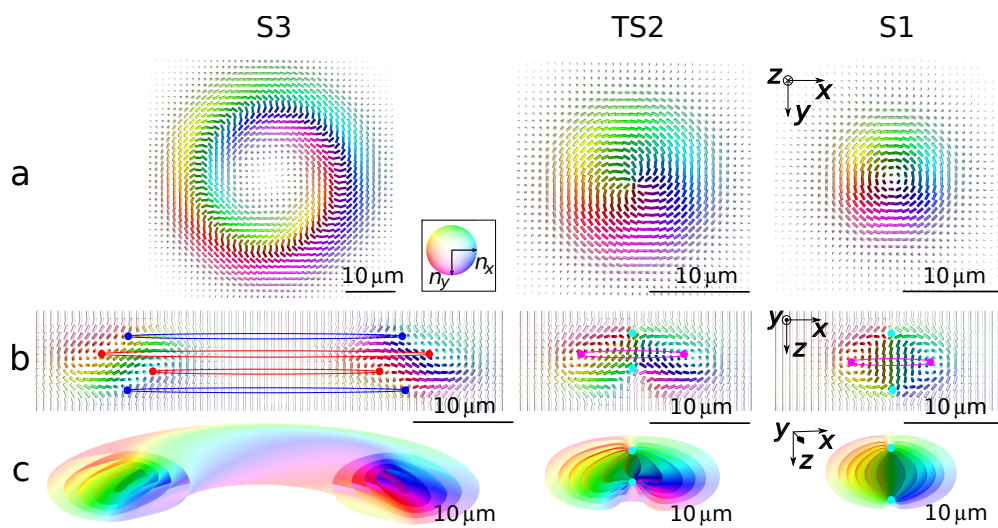

Figure 2. Director fields and topology of S3 (looped CF1 finger), TS2 (transient structure), and S1 (toron). (**a**,**b**) Orientational structures in the xy and xz planes, respectively. (**c**) Isosurfaces of the z projection of the director computed at $n_z \in \{\pm 0.83, \pm 0.5, \pm 0.17\}$. For S3, a pair of $\lambda^{+1/2}$ ($\lambda^{-1/2}$) disclination loops is marked by red (blue) circles. For TS2 and S1, cyan (magenta) circles indicate two hyperbolic hedgehogs (+1 disclination ring).

3.2. Analytical Design of Localized Topological Structures

In this section, the CLC director is modeled using analytical tools formulated in terms of formulas representing various helicoidal CLC structures and serving as elementary buildings blocks for topological solitons. From the above discussion, the S3 structure is a looped cholesteric finger CF1 that contains approximately one period of the tilted helix embedded into the uniform vector field. Therefore, the principal building block for our ansatz is a straight CF1 [45].

A uniform helical structure with the helix axis along the unit vector $\hat{\mathbf{q}}$

$$\mathbf{n}(\mathbf{r}) = \hat{\mathbf{a}} \cos \psi + \hat{\mathbf{b}} \sin \psi, \quad \psi = 2\pi(\mathbf{r} \cdot \hat{\mathbf{q}})/P, \tag{6}$$

where a hat indicates unit vectors; $\hat{\mathbf{a}}$ and $\hat{\mathbf{b}} = \hat{\mathbf{q}} \times \hat{\mathbf{a}}$ are unit vectors orthogonal to $\hat{\mathbf{q}}$; and P is the helix pitch, presents the simplest case of helical structure that is the ground-state structure for unbounded CLCs provided $2\pi/P$ is the free twisting number.

In order to transform the tilted helix to CF1, we can add the uniform homeotropic structure $\hat{z}$ multiplied by weight function m, and normalize the resulting vector field as follows:

$$\mathbf{N} = \mathbf{n} + m(\mathbf{r})\hat{z}, \quad \hat{\mathbf{n}}(\mathbf{r}) = \frac{\mathbf{N}(\mathbf{r})}{|\mathbf{N}(\mathbf{r})|}. \tag{7}$$

We assume that the weight is a smooth function. Inside the cholesteric finger, the weight vanishes, whereas it grows in the regions where the director field is nearly homeotropic. For instance, let us consider the weight written as a sum of three terms $m = m_{\text{surf}} + m_{+,\text{helix}} + m_{-,\text{helix}}$ given by

$$m_{\text{surf}} = \left[\frac{2d}{L-2z}\right]^p + \left[\frac{2d}{L+2z}\right]^p, \tag{8}$$

$$m_{\pm,\text{helix}} = \exp(\gamma(\pm\mathbf{r}\cdot\hat{\mathbf{q}} - \rho)), \tag{9}$$

where m_{surf} is infinitely large at the substrates and $m_{+,\text{helix}}$ ($m_{-,\text{helix}}$) grows exponentially in the half-space $\mathbf{r}\cdot\hat{\mathbf{q}} > \rho$ ($\mathbf{r}\cdot\hat{\mathbf{q}} < -\rho$).

Coefficient function (8) with positive parameters d and p is used to modify the director field so as to meet the rigid homeotropic anchoring conditions. The width of the surface layer is determined by parameter d, whereas parameter p is related to the rate of director reorientation near the surface. All our subsequent calculations were performed at $d = 1.1$ μm and $p = 2$. Similarly, in Equation (9), the width of the finger and the gradient of the director varying from the finger to the uniform phase are governed by the parameters ρ and γ, respectively.

Figure 3 shows the cholesteric finger modeled using ansatz (7) and weight functions (8)–(9) with $P = 15$ μm, $\hat{\mathbf{q}} = (1,0,1)/\sqrt{2}$, $\gamma = 0.7$ μm^{-1} and $\rho = 8$ μm. If $\hat{\mathbf{q}}$ is not orthogonal to $\hat{z}$, the construction does not produce point defects, since $\mathbf{N}$ is never zero. Referring to Figure 3, we also had two pairs of nonsingular disclination lines as expected. These disclinations are marked by the points on the xz cross-section in Figure 3.
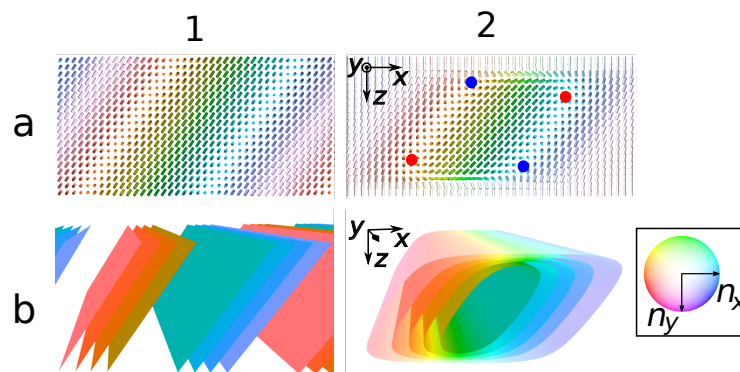

Figure 3. Director field distributions of (1) tilted helix (see Equation (6)) and (2) cholesteric finger CF1 (see Equation (7)) computed for the case of straight cholesteric finger. (**a**) Vertical cross-section of the director field. (**b**) Isosurfaces of the z-projection of the director. Blue and red points indicate disclination lines.

Equation (6) can also be used to introduce a more complicated helical configurations by replacing the Cartesian coordinates with the curvilinear ones. So, in order to define the looped helix, we employed the cylindrical coordinate system with radial distance $\rho = \sqrt{x^2 + y^2}$ and azimuthal angle ϕ, $\tan\phi = y/x$. By assuming that angle Φ between $\hat{z}$ and the helix axis is fixed, we have

$$\hat{\mathbf{q}} = \hat{\rho}\sin\Phi + \hat{z}\cos\Phi, \quad \hat{\mathbf{a}} = \hat{\rho}\cos\Phi - \hat{z}\sin\Phi, \quad \hat{\mathbf{b}} = \hat{\boldsymbol{\phi}}, \tag{10}$$

where $\hat{\boldsymbol{\rho}} = \hat{\mathbf{x}}\cos\phi + \hat{\mathbf{y}}\sin\phi$ and $\hat{\boldsymbol{\phi}} = -\hat{\mathbf{x}}\sin\phi + \hat{\mathbf{y}}\cos\phi$. The looped helix can now be defined as the vector field:

$$\mathbf{S} = \hat{\mathbf{a}}\cos\psi + \hat{\mathbf{b}}\sin\psi, \quad \psi = \frac{2\pi c}{P}, \tag{11}$$

where $\{a, b, c\} = \{-z\sin\Phi + \rho\cos\Phi, \phi, z\cos\Phi + \rho\sin\Phi\}$ are our curvilinear coordinates.

For helix $\mathbf{S}$, all points of line $\rho = 0$ are singular. However, such defects are unstable, and relaxation transforms them into isolated point defects. In order to model these point defects, we modified the looped helix $\mathbf{S}$ by adding similarly organized structure $\mathbf{S}' = \mathbf{S}(-\rho, \phi + \pi)$. In other words, structure $\mathbf{S}'$ was obtained from $\mathbf{S}$ when the inplane projection of the director $\mathbf{S} - (\mathbf{S} \cdot \hat{\mathbf{z}})\hat{\mathbf{z}}$ and the coordinate ρ that entered phase ψ changed their signs. Field $\mathbf{S} + \mathbf{S}'$ is continuous with the director aligned along $\hat{\mathbf{z}}$ on the symmetry axis $\rho = 0$. Point defects are formed when this field vanishes and cannot be normalized. These singular points are hyperbolic and represent the hedgehogs shown in Figure 2.

The general form of the ansatz for topological solitons is a linear combination of the homeotropic structure $\hat{\mathbf{z}}$ and the helix $\mathbf{S}'$ superimposed with $\mathbf{S}$ as follows:

$$\mathbf{N} = \mathbf{S} + m'(\mathbf{r})\mathbf{S}' + m(\mathbf{r})\hat{\mathbf{z}}, \quad \hat{\mathbf{n}}(\mathbf{r}) = \frac{\mathbf{N}(\mathbf{r})}{|\mathbf{N}(\mathbf{r})|}, \tag{12}$$

where $m'(\mathbf{r})$ and $m(\mathbf{r})$ are the coefficient functions that are expressed in terms of m_{surf}, given by Equation (8), and the two following weight (mask) functions:

$$m_{\text{cone}}^{(\pm)} = m_{\pm}(\Phi) + m_{\mp}(-\Phi), \tag{13}$$

$$m_{\pm}(\Phi) = \exp(\pm\kappa(c(\Phi) - |\sin\Phi|s)), \tag{14}$$

$$m_{\text{as}} = e^{-\alpha\rho/2}, \tag{15}$$

where $m_{\pm}$ can be regarded as a modified version of Equation (9). Similar to the cholesteric finger (7), weight m is a smooth function chosen to be close to zero within the region of the solitonic structure localization. When the structure is nearly homeotropic, the weight is large.

With the help of the function given by the first term on the right-hand side of Equation (14), we cut all periods of the helical structures with $c > s$. The sharpness of the cut is governed by the parameter $\kappa > 0$, which was taken to be $\kappa = 0.7$.

Formula (15) gives coefficient function m_{as}, used to transition from the uniform helix at $\rho = 0$ to the oblique helix.

Structure S3 is the simplest that could be obtained from a looped helix by removing everything except for approximately one period and immersing the result into a uniform phase. It is given by

$$\mathbf{N}_{\text{S3}} = \mathbf{S} + \left(m_{\text{surf}} + m_{\text{cone}}^{(+)}\big|_{s=\rho_1} + m_{\text{cone}}^{(-)}\big|_{s=\rho_0}\right)\hat{\mathbf{z}}, \tag{16}$$

where ρ_0 and ρ_1 are the inner and outer radii of $S3$, respectively. An important feature of S3 is the uniformly oriented inner region; thus, the remaining part of the helix should not intersect the axis of symmetry $\rho_0 > 0$. So, there are no defects on axis $\rho = 0$ that need to be regularized using $\mathbf{S}'$.

The chirality of the POM texture for S3 manifested itself in spiral arms marked as Region III in Figure 4. It occurred due to nonzero curvature of the looped helix. The bright rings (see Regions I and II in Figure 4) bounding the spiral arms are more difficult to model. Inspecting the director field presented in Figure 1d shows that the ends of the cholesteric finger are wedge shaped having both side non parallel to the substrates. In our ansatz, we took this observation into account by masking everything outside outer and inside inner radii using weight functions $m_{\text{cone}}^{\pm}$, where each mask involved two cuts by cones $m_{\pm}(+\Phi)$ and $m_{\pm}(-\Phi)$ with the opposite slopes $\pm\Phi$.
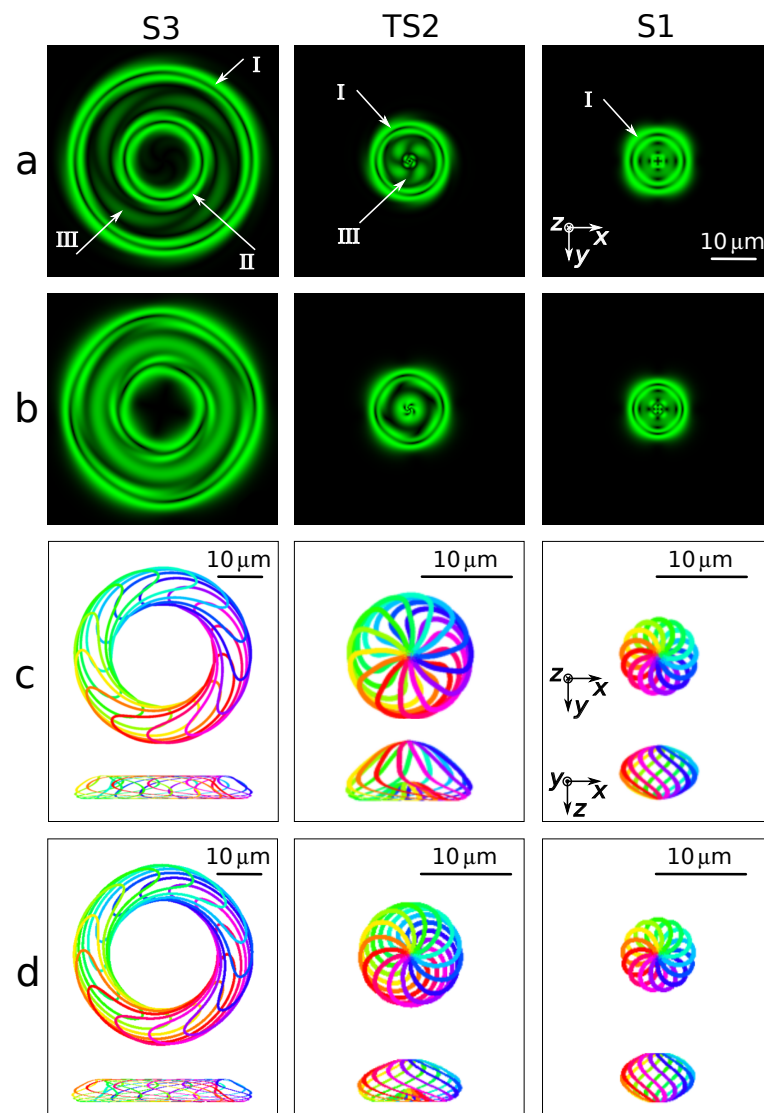
Figure 4. Approximated and simulated POM textures and director field distributions for localized topological structures S3, TS2, and S1. (**a**,**c**) Results for approximated (designed) structures using analytical ansatz (12) (see text for the list of parameters). (**b**,**d**) Results for the simulated structures from the lattice model. (**a**,**b**) Green light POM images in crossed polarizers at the 532 nm wavelength for $n_e = 1.76$ and $n_o = 1.53$. Orientation of the axes and the white scale bar for (**a**,**b**) are shown in the inset at the left and the right of the texture for S1, respectively. (**c**,**d**) Isolines for the z projection of the director in the xy and the xz planes. Orientation of the axes for (**c**,**d**) is shown in the insets at the left of the distributions for S1. Chiral arms are marked as Region III, whereas Regions I and II indicate outer and inner bright rings, respectively.

The transformation of the cholesteric finger into structure S3 rendered the four disclination lines looped and did not produce point defects. Structure TS2 was formed when the inner radius of S3 became smaller than zero. The part of the director field that was not aligned along $\hat{\mathbf{z}}$ filled a thickened cone, and defects were formed near the apex of the cone. The looped helix, which was the main ingredient of our ansatz, produced a line defect that was unstable and decayed into the two point defects shown in Figure 2. To mimic the behavior, we added regularizing field $\mathbf{S}'$ with weight m_{as} that equaled unity at the axis of symmetry and decayed fast. For TS2, the ansatz reads

$$\mathbf{N}_{TS2} = \mathbf{S} + m_{\text{as}}\big|_{\alpha=-0.5}\mathbf{S}' + (m_{\text{surf}} + m_{\text{cone}}^{(+)}\big|_{s=\rho_1})\hat{\mathbf{z}}, \tag{17}$$

where ρ_1 is the radius of the topological soliton. When S3 shrank, producing TS2, disclinations may have also been transformed into point defects. Though the exact number of generated point defects may depend on details of the structure, we restricted ourselves to the case of two point defects supported by the results of our numerical simulations shown in Figure 2. The central part of the POW texture was sensitive to the distance between the point defects. This distance was tuned by the change in coordinate $c \to c + \Delta c$.

In contrast to S3 and TS2, the POM image of S1 was achiral. From the director field (see Figures 1 and 2), this is a consequence of the symmetry of the structure that was invariant under reflection: $z \mapsto -z$. The ansatz for S1

$$\mathbf{N}_{S1} = \mathbf{S} + \mathbf{S}' + (m_{\mathrm{surf}} + m_{\mathrm{cone}}^{(+)}\big|_{s=\rho_1})\hat{\mathbf{z}} \tag{18}$$

was similar to that of TS2, but the reflection symmetry required the weight of the reflected looped helix $\mathbf{S}'$ to be equal to unity. If radius ρ_1 was sufficiently small, the resulting structure had two hyperbolic point defects (hyperbolic hedgehogs) on the z axis, $\rho = 0$, and one disclination line in plane $z = 0$. This is exactly the topology of a toron.

3.3. Approximated Structures

In Figure 4, we compare the results computed for the lattice model using the energy minimization procedure with the results for the structures analytically designed using ansatz (12) with suitably defined coefficient functions for each localized structure. The weight functions serve only the purpose of ensuring a smooth transition between the uniform phase and the cholesteric finger. Otherwise, there is freedom in the choice of the analytical expressions of these functions. The remaining parameters, such as the helical pitch and the tilt angle of the cholesteric finger, were recovered from the director fields obtained with the relaxation procedure described above.

Now, we list the parameters used in calculations based on the ansatz. For the looped (conically packed) helix (see Equation (11)) describing structure S1, the pitch and tilt angles of the twisting axis are given by the following relations: $P = 15\ \mu\mathrm{m}$ and $\tan \Phi = 0.7$, whereas the radius of the soliton is $\rho_1 = 7\ \mu\mathrm{m}$. In the case of structure TS2, these parameters are: $P = 12\ \mu\mathrm{m}$, $\tan \Phi = 0.9$, $\rho_1 = 10\ \mu\mathrm{m}$ and $\Delta c = 2.5\ \mu\mathrm{m}$. For S3, we have $P = 12\ \mu\mathrm{m}$ and $\tan \Phi = 0.7$, whereas the inner and the outer soliton radii are $\rho_0 = 5\ \mu\mathrm{m}$ and $\rho_1 = 23\ \mu\mathrm{m}$, respectively.

A comparison of Figure 4a,b shows that the simulated and approximated textures are in reasonable agreement. For the cases of S1 and S3, agreement between the textures was excellent, whereas for TS2, the fine details of the lobes in the central dark part of the simulated texture were not perfectly reproduced in the approximated counterpart.

In Figure 4c,d, the director field distributions are illustrated with the help of isolines where the component of the director along the cell normal, n_z, was constant. These isolines could be described as preimages with the same polar angles but different azimuthal angles [30]. Differences between the simulated and approximated isolines in both the xy and xz planes were hard to spot by the naked eye. So, we arrived at the conclusion that topologies of the simulated and the approximated director fields were identical.

Director field engineering described in Section 3.2 can be regarded as a multistep procedure. In Figure 5, we consider structure S1 and detail the results for each intermediate step of analytical design. These steps were determined with the coefficient functions that entered ansatz (18). Columns in Figure 5 present the POM texture and the distributions of the azimuthal director angle in the xy and xz planes evaluated at each step. For instance, the results for the looped helix are shown in the the first column, and the subsequent two columns show what happened when different parts of the helix were eliminated.

In Figure 6, we see how the pitch and twisting axis tilt of the helix (11) influence the approximated POM images for structure S3. An important point that is demonstrated in Figure 6 is that the POM textures of topologically equivalent structures may reveal considerable differences.
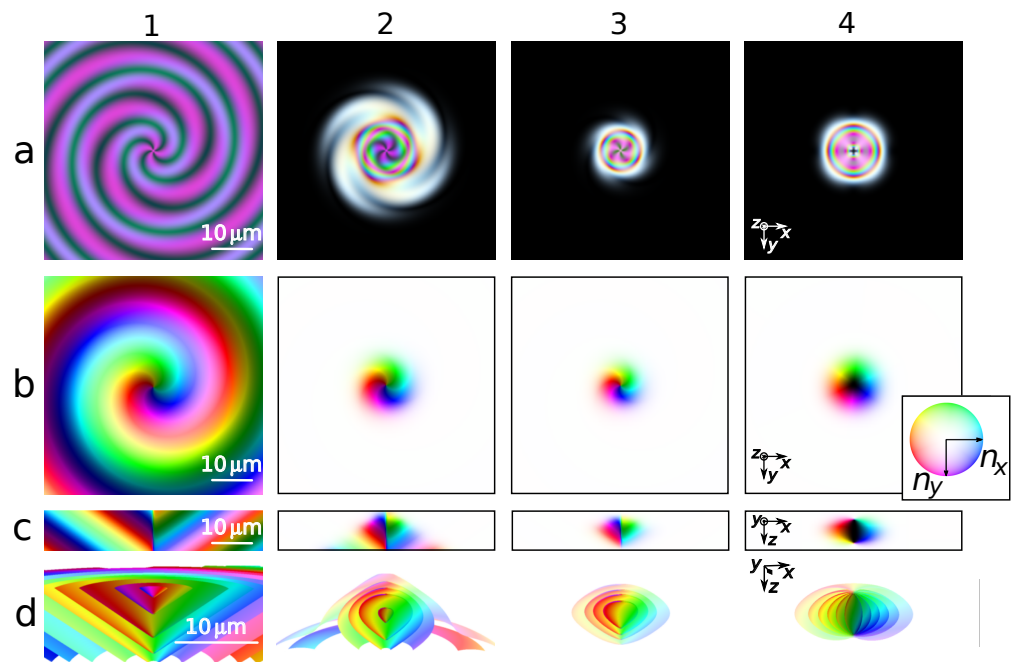
Figure 5. POM images and director field distributions of structure S1 approximated using different ansatz functions in Equation (18): (1) $\mathbf{N} = \mathbf{S}$; (2) $\mathbf{N} = \mathbf{S} + m_{+}(\Phi)\hat{\mathbf{z}}$; (3) $\mathbf{N} = \mathbf{S} + m_{\text{cone}}^{(+)}\hat{\mathbf{z}}$; (4) $\mathbf{N} = \mathbf{S} + \mathbf{S}' + (m_{\text{surf}} + m_{\text{cone}}^{(+)})\hat{\mathbf{z}}$. (**a**) White light POM textures seen in crossed polarizers at $n_e = 1.76$ and $n_o = 1.53$. (**b**) Director field distributions in the xy plane (the origin is at the center of the cell). (**c**) Director field distributions in the xz plane (the origin is at the center of the cell). (**d**) Isosurfaces of the z projection of the director computed at $n_z \in \{\pm 0.83, \pm 0.5, \pm 0.17\}$. The helix pitch is $P = 15$ µm and $\tan \Phi = 0.7$, where Φ is the helix tilt angle.
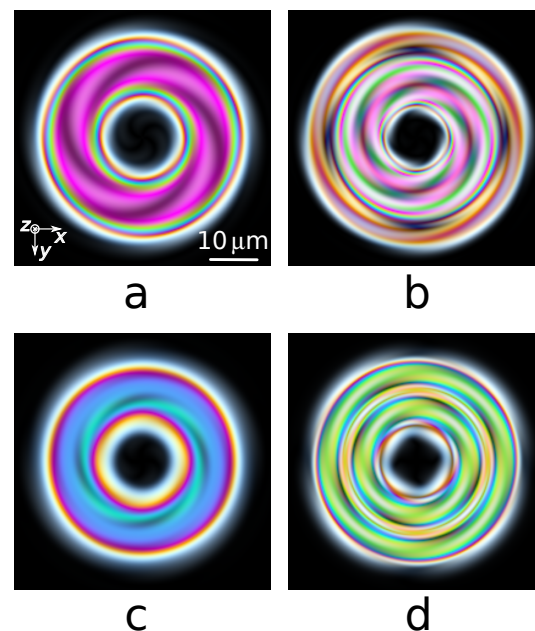

Figure 6. White-light POM images in crossed polarizers for the structure S3 approximated using ansatz (16) with varying pitch P and helix tilt angle Φ. (**a**) $P = 12$ µm and $\tan \Phi = 0.7$ (see Figure 2); (**b**) $P = 12$ µm and $\tan \Phi = 1.4$; (**c**) $P = 6$ µm and $\tan \Phi = 0.7$; (**d**) $P = 6$ µm and $\tan \Phi = 1.4$; Other parameters are: $n_e = 1.76$, $n_o = 1.53$, $\rho_0 = 5$ µm and $\rho_1 = 23$ µm.

4. Conclusions

In this paper, we used numerical modeling and the analytical design approaches to study the director field distributions and the corresponding POM textures of the localized

solitonic CLC structures S1, TS2 and S3. The simulated director fields were computed for the lattice model by means of the energy minimization procedure. In the analytical design approach, we approximated the director field using the ansatz of the general form given by Equation (12).

Both the ansatz and the simulation led to perfectly identical results as far as the director field topology of the structures under consideration was concerned. For S1 and S3, the approximated and simulated POM textures were in good agreement. Structure TS2 presented the only case where, though the textures are in reasonable agreement, the differences were noticeable. One of the reasons for that was that this structure turned out to be sensitive to the boundary conditions.

Our director field design can be divided into several steps that take into account different factors and suitably modify the director pattern. In Figure 5, we show the effects produced at each step.

The most important parameters that entered our ansatz were the helix pitch and tilt of the cholesteric finger. We used the director field measurements to fit these parameters. An alternative approach is to minimize free energy with respect to the parameters. Though the ansatz wsas too complex to analytically treat the free energy, numerical simulations can be performed to adjust parameters.

In principle, there are alternative scenarios to the S3-to-S1 transition that might be more complicated than the simulated one. In order to deal with such scenarios, more accurate analysis may require to replace the elasticity theory on the basis of Frank free energy (this theory can safely be used to describe our case) with the Landau–de Gennes theory for the order parameter tensor. Our analysis of optical properties can also be improved by going beyond the well-known limitations of the Jones matrix method.

Our concluding remark is that, although topologically equivalent structures can be optically different, the suggested ansatz correctly captured the geometry and optical properties of the studied structures. Since these structures are relatively easy to generate in experiments, using this ansatz may significantly simplify the analysis of the experimental data. The extension of the analytical approach to the case of structures with linked preimages such as hopfions is the subject of our future research.

Author Contributions: I.L.: conceptualization, methodology, software; E.A.: investigation, visualization; T.O.: validation, writing—original draft; D.D.: data curation; V.U.: conceptualization, methodology, supervision; A.D.K.: methodology, writing—review and editing. All authors have read and agreed to the published version of the manuscript.

Institutional Review Board Statement: Not applicable.

Informed Consent Statement: Not applicable.

Data Availability Statement: Not applicable.

Conflicts of Interest: The authors declare no conflict of interest.

Sample Availability: Not applicable.

References

1. Haas, W.E.L.; Adams, J.E. Electrically variable diffraction in spherulitic liquid crystals. *Appl. Phys. Lett.* **1974**, *25*, 263–264. [CrossRef]
2. Kawachi, M.; Osamu Kogure, O.; Kato, Y. Bubble domain texture of a liquid crystal. *Jpn. J. Appl. Phys.* **1974**, *13*, 1457. [CrossRef]
3. Hamdi, R.; Petriashvili, G.; Lombardo, G.; De Santo, M.P.; Barberi, R. Liquid crystal bubbles forming a tunable micro-lenses array. *J. Appl. Phys.* **2011**, *110*, 074902. [CrossRef]

4. Yang, B.; Brasselet, E. Arbitrary vortex arrays realized from optical winding of frustrated chiral liquid crystals. *J. Opt.* **2013**, *15*, 044021. [CrossRef]
5. Hess, A.J.; Poy, G.; Tai, J.S.B.; Žumer, S.; Smalyukh, I.I. Control of Light by Topological Solitons in Soft Chiral Birefringent Media. *Phys. Rev. X* **2020**, *10*, 031042. [CrossRef]
6. Ackerman, P.J.; Qi, Z.; Smalyukh, I.I. Optical generation of crystalline, quasicrystalline, and arbitrary arrays of torons in confined cholesteric liquid crystals for patterning of optical vortices in laser beams. *Phys. Rev. E* **2012**, *86*, 021703. [CrossRef]
7. Ackerman, P.J.; Mundoor, H.; Smalyukh, I.I.; Van De Lagemaat, J. Plasmon–Exciton Interactions Probed Using Spatial Coentrapment of Nanoparticles by Topological Singularities. *ACS Nano* **2015**, *9*, 1239–12400. [CrossRef]
8. Evans, J.S.; Ackerman, P.J.; Broer, D.J.; van de Lagemaat, J.; Smalyukh, I.I. Optical generation, templating, and polymerization of three-dimensional arrays of liquid-crystal defects decorated by plasmonic nanoparticles. *Phys. Rev. E* **2013**, *87*, 032503. [CrossRef]
9. Saberi-Pouya, S.; Conti, S.; Perali, A.; Croxall, A.F.; Hamilton, A.R.; Peeters, F.M.; Neilson, D. Experimental conditions for the observation of electron-hole superfluidity in GaAs heterostructures. *Phys. Rev. B* **2020**, *101*, 140501. [CrossRef]
10. Ribiere, P.; Pirkl, S.; Oswald, P. Electric-field-induced phase transitions in frustrated cholesteric liquid crystals of negative dielectric anisotropy. *Phys. Rev. A* **1991**, *44*, 8198. [CrossRef]
11. Oswald, P.; Baudry, J.; Pirkl, S. Static and dynamic properties of cholesteric fingers in electric field. *Phys. Rep.* **2000**, *337*, 67–96. [CrossRef]
12. Afghah, S.; Selinger, J.V. Theory of helicoids and skyrmions in confined cholesteric liquid crystals. *Phys. Rev. E* **2017**, *96*, 012708. [CrossRef]
13. Durey, G.; Sohn, H.R.O.; Ackerman, P.J.; Brasselet, E.; Smalyukh, I.I.; Lopez-Leon, T. Topological solitons, cholesteric fingers and singular defect lines in Janus liquid crystal shells. *Soft Matter* **2020**, *16*, 2669. [CrossRef]
14. Ackerman, P.J.; Smalyukh, I.I. Diversity of Knot Solitons in Liquid Crystals Manifested by Linking of Preimages in Torons and Hopfions. *Phys. Rev. X* **2017**, *7*, 011006. [CrossRef]
15. Smalyukh, I.I.; Lansac, Y.; Clark, N.A.; Trivedi, R.P. Three-dimensional structure and multistable optical switching of triple-twisted particle-like excitations in anisotropic fluids. *Nat. Mater.* **2010**, *9*, 139–145. [CrossRef]
16. Loussert, C.; Brasselet, E. Multiple chiral topological states in liquid crystals from unstructured light beams. *Appl. Phys. Lett.* **2014**, *104*, 051911. [CrossRef]
17. Shvetsov, S.; Orlova, T.; Emelyanenko, A.V.; Zolot'ko, A. Thermo-Optical Generation of Particle-Like Structures in Frustrated Chiral Nematic Film. *Crystals* **2019**, *9*, 574. [CrossRef]
18. Loussert, C.; Iamsaard, S.; Katsonis, N.; Brasselet, E. Subnanowatt Opto-Molecular Generation of Localized Defects in Chiral Liquid Crystals. *Adv. Mater.* **2014**, *26*, 4242–4246. [CrossRef]
19. Orlova, T.; Lancia, F.; Loussert, C.; Iamsaard, S.; Katsonis, N.; Brasselet, E. Revolving supramolecular chiral structures powered by light in nanomotor-doped liquid crystals. *Nat. Nanotechnol.* **2018**, *13*, 304–308. [CrossRef]
20. Orlova, T.; Iegorov, R.; Kiselev, A.D. Light-induced pitch transitions in photosensitive cholesteric liquid crystals: Effects of anchoring energy. *Phys. Rev. E* **2014**, *89*, 012503. [CrossRef]
21. Chen, B.G.G.; Ackerman, P.J.; Alexander, G.P.; Kamien, R.D.; Smalyukh, I.I. Generating the Hopf Fibration Experimentally in Nematic Liquid Crystals. *Phys. Rev. Lett.* **2013**, *110*, 237801. [CrossRef]
22. Trivedi, R.P.; Lee, T.; Bertness, K.A.; Smalyukh, I.I. Three dimensional optical manipulation and structural imaging of soft materials by use of laser tweezers and multimodal nonlinear microscopy. *Opt. Express* **2010**, *18*, 27658–27669. [CrossRef]
23. Pirkl, S.; Ribiere, P.; Oswald, P. Forming process and stability of bubble domains in dielectrically positive cholesteric liquid crystals. *Liq. Cryst.* **1993**, *13*, 413–425. [CrossRef]
24. Shen, Y.; Dierking, I. Electrically driven formation and dynamics of skyrmionic solitons in chiral nematics. *Phys. Rev. Appl.* **2021**, *15*, 054023. [CrossRef]
25. Ackerman, P.J.; Trivedi, R.P.; Senyuk, B.; van de Lagemaat, J.; Smalyukh, I.I. Two-dimensional skyrmions and other solitonic structures in confinement-frustrated chiral nematics. *Phys. Rev. E* **2014**, *90*, 012505. [CrossRef]
26. Smalyukh, I.I.; Zribi, O.V.; Butler, J.C.; Lavrentovich, O.D.; Wong, G.C. Structure and Dynamics of Liquid Crystalline Pattern Formation in Drying Droplets of DNA. *Phys. Rev. Lett.* **2006**, *96*, 177801. [CrossRef]
27. Posnjak, G.; Čopar, S.; Muševič, I. Hidden topological constellations and polyvalent charges in chiral nematic droplets. *Nat. Commun.* **2017**, *8*, 14594. [CrossRef]
28. Fernandez-Nieves, A.; Puertas, A.M. *Fluids, Colloids and Soft Materials: An Introduction to Soft Matter Physics*; John Wiley & Sons, Inc.: Hoboken, NJ, USA, 2016; pp. 165–186.
29. Wu, J.-S.; Smalyukh, I.I. Hopfions, heliknotons, skyrmions, torons and both abelian and nonabelian vortices in chiral liquid crystals. *Liq. Cryst. Rev.* **2022**, 1–35. [CrossRef]
30. Smalyukh, I.I. Review: Knots and other new topological effects in liquid crystals and colloids. *Rep. Prog. Phys.* **2020**, *83*, 106601. [CrossRef]
31. Kougo, J.; Araoka, F.; Haba, O.; Yonetake, K.; Aya, S. Photo-reconfigurable twisting structure in chiral liquid crystals triggered by photoresponsive surface. *J. Chem. Phys.* **2021**, *155*, 061101. [CrossRef]
32. de Gennes, P.G.; Prost, J. *The Physics of Liquid Crystals*; Clarendon Press: Oxford, UK, 1993.
33. Tambovtsev, I.M.; Leonov, A.O.; Lobanov, I.S.; Kiselev, A.D.; Uzdin, V.M. Topological structures in chiral media: Effects of confined geometry. *Phys. Rev. E* **2022**, *105*, 034701. [CrossRef]

34. Lobanov, I.; Uzdin, V. The lifetime of micron scale topological chiral magnetic states with atomic resolution. *Comput. Phys. Commun.* **2021**, *269*, 108136. [CrossRef]

35. Lobanov, I.; Potkina, M.; Uzdin, V. Stability and lifetimes of magnetic states of nano- and microstructures (Brief Review). *JETP Lett.* **2021**, *113*, 801. [CrossRef]

36. Trabi, C.L.; Brown, C.V.; Smith, A.A.T.; Mottram, N.J. Interferometric method for determining the sum of the flexoelectric coefficients (e1+e3) in an ionic nematic material. *Appl. Phys. Lett.* **2008**, *92*, 223509. [CrossRef]

37. Strömer, J.F.; Raynes, E.P. Study of elastic constant ratios in nematic liquid crystals. *Appl. Phys. Lett.* **2006**, *88*, 051915. [CrossRef]

38. Raynes, E.P.; Brown, C.V.; Strömer, J.F. Method for the measurement of the K_{22} nematic elastic constant. *Appl. Phys. Lett.* **2003**, *82*, 13–15. [CrossRef]

39. Wang, H.; Wu, T.X.; Gauza, S.; Wu, J.R.; Wu, S.T. A method to estimate the Leslie coefficients of liquid crystals based on MBBA data. *Liquid Cryst.* **2006**, *33*, 91–98. [CrossRef]

40. Yeh, P.; Gu, C. *Optics of Liquid Crystal Displays*; Wiley: New York, NY, USA, 1999; p. 438.

41. Ellis, P.W.; Pairam, E.; Fernández-Nieves, A. Simulating optical polarizing microscopy textures using Jones calculus: A review exemplified with nematic liquid crystal tori. *J. Phys. D Appl. Phys.* **2019**, *52*, 213001. [CrossRef]

42. Baudry, J.; Pirkl, S.; Oswald, P. Topological properties of singular fingers in frustrated cholesteric liquid crystals. *Phys. Rev. E* **1998**, *57*, 3038. [CrossRef]

43. Smalyukh, I.I.; Senyuk, B.I.; Palffy-Muhoray, P.; Lavrentovich, O.D.; Huang, H.; Gartland, E.C.; Bodnar, V.H.; Kosa, T.; Taheri, B. Electric-field-induced nematic-cholesteric transition and three-dimensional director structures in homeotropic cells. *Phys. Rev. E* **2005**, *72*, 061707. [CrossRef]

44. Li, J.; Wen, C.H.; Gauza, S.; Lu, R.; Wu, S.T. Refractive indices of liquid crystals for display applications. *J. Disp. Technol.* **2005**, *1*, 51–61. [CrossRef]

45. Gil, L.; Gilli, J.M. Surprising dynamics of some cholesteric liquid crystal patterns. *Phys. Rev. Lett.* **1998**, *80*, 5742. [CrossRef]